Spray production and surface foam longevity under breaking waves

Chris Chickadel, Bill Asher
Applied Physics Laboratory, University of Washington
1013 NE 40th Street, Seattle WA 98105
phone: (206) 221-7673 fax: (206) 616-3142 email: chickadel@apl.uw.edu

Award Number: N00014-15-1-2719
http://apl.washington.edu

Objectives

The overall objective is to understand and quantify the spray production and longevity of surface foam produced by deep-water whitecaps, depth-limited breaking in surf zones, and ship wakes. The specific objectives are to:

- Quantify the spray distribution and flux from field scale saltwater breaking waves
- Determine the role of turbulence in regulating sea foam longevity at the surface

Motivation and Background

Wave breaking produces one of the largest electromagnetic (EM) signals used for remote sensing of the ocean environment. The increase in backscatter and/or emissivity by the aerated portion of the breaking wave (i.e., wave roller) and residual foam are easily detected by microwave, infrared, and visible remote sensing modes. Spray produced by breaking waves also affects EM propagation in the atmosphere above the ocean, limiting visibility and distorting signal propagation by contributing to atmospheric ducting of EM waves in the marine boundary layer (MBL).

The foam patch generated by a whitecap, surf zone wave, or ship wake develops in two phases. The initial "active phase" [*Deane and Stokes*, 2002] is defined by the initial entrainment of air, which happens when the wave collapses and air is injected into the wave face. This is also when the main turbulent kinetic energy (TKE) is injected into the water column [*Gemmrich*, 2010]. This TKE and the jet that is formed during the entraining process forces bubbles down and breaks larger bubbles into smaller bubbles [*Deane and Stokes*, 2002]. Below a diameter of approximately 1 mm, bubbles are submerged more easily in the ambient turbulence, while larger bubbles with higher buoyancy rise to the surface with velocities on order of 10 cm s^{-1} [*Callaghan*, 2013].

The rise of bubbles back to the surface after their entrainment is terms the decaying phase of the surface foam. This process is influenced by the TKE (both generated by the breaking process, and the TKE present before breaking began) and bubble surface chemistry [*Callaghan et al.,* 2013]. Surfactants can lengthen the time decay of the residual foam patch by decreasing the rise velocities of individual bubbles and by extending the life of bubbles on the water surface [*Asher et al.,* 1997], However, the effect of wave turbulence and wave energy dissipation on the decay phase of a foam patch has not been measured directly. *Callaghan et al.* [2013] and *Callaghan* [2013] show that foam patch lifetime is a function of wave slope and wind speed, with lifetime increasing with steepness and wind speed. Because the TKE of the breaking process increases with both steepness and wind speed, this suggests that higher wave energies result in longer foam decay times.

Sea spray droplets are produced from bursting bubbles, splashes during breaking, and through spume production where the wind stress shears off wave crests. During formation, these droplets diameters range in size from 1 μm to 1000 μm, with most drops having diameters of less than 2 μm [*Andreas et al.* 1995; *Mårtensson et al. 2003*]. Modeling the optical properties of the marine boundary layer MBL requires knowledge of the flux of droplets from the ocean to the atmosphere in terms of the number of particles of given radius per unit of ocean surface area per increment of radius, otherwise known as the sea spray generation function (SSGF). There are a multitude of SSGFs including ones parameterized using whitecap coverage [*Monahan et al*. 1986], wind speed [*Andreas et al.* 1995], turbulent fluxes [*Greever et al.* 2005; *Nilsson et al*. 2001], and gradient flux methods [*Petelski and Piskozub,* 2006]. Unfortunately, there is no general consensus on the applicability or accuracy of these spray models because measurements of foam and spray needed to test them are usually provided by laboratory experiments or through limited field observations. Field observations are troublesome since the droplet number size density distributions, $n(r)$ (i.e., the number of particles of given radius per unit volume of air per increment of radius, r, from which the SSGF is derived) measured under similar conditions, but by different researchers differ by orders of magnitude [*de Leeuw et al*. 2011]. Laboratory simulations using foam generators and small-scale breaking waves do not fully represent the energetics (turbulence) and volume of air entrained by the larger wave breaking processes in the field. Furthermore, field measurements are usually performed at significant height above the sea surface (several meters at least) so that the SSGF is not directly sampled.

Technical Approach

Using a combination of imaging, laser techniques, and in situ observations we measured wave breaking and spray generation of breaking waves in the Ohmsett wave tank, a 200-m long saltwater wave flume located at Naval Weapons Station Earle in Monmouth, NJ. The instruments were mounted on a vertical frame to a movable bridge that spanned the tank, thus the position of the instruments could be moved relative to the location of the breaking wave (Figure 1). Waves were generated using a focused wave packet technique [*Rapp and Melville,* 1990] with Observations were made of repeated waves under a variety of breaking wave conditions.

The sea spray was measured within 1 m of the breaking wave surface using a phase-Doppler anemometer (PDA) for droplets between 0.1μm and 100 μm. This size range comprises both the range where the number-size distribution reaches its maximum and represents most of the spray droplet mass flux [*Andreas et al.* 1995]. A PDA, in similarity with laser-Doppler velocimeters, measures the velocity of a moving particle. However, a PDA also measures particle size [*Asher and Farley*, 1995]. Phase-Doppler anemometry uses the principle that when the same scattering event is viewed at two different locations each location records the same Doppler burst frequency. However, there is a phase difference, ϕ, between the two Doppler burst signals due to the difference in optical path to the detectors. Assuming the scattering geometry remains constant, ϕ is a function of r, droplet radius, [*Bauckhage et al.*, 1988] and the phase difference can be exploited to allow measurement of r. *Naqwi and Ziema* [1992] and [*Göbel et al.*, 1998] have shown how PDA can be used to measure particles with r as small as 0.1 μm. A PDA produces a time series of the sizes of individual particles that can be used to calculate $n(r)$ using the method described by *Qiu and Sommerfeld* [1992] and *Asher and Farley* [1995].

To observe large drop (> 100 μm) and bubbles a pair of monochrome visible cameras were mounted in submersible housings above and below the waterline, respectively. Telecentric macro lenses were installed on the cameras to limit perspective distortion within the field of view of the cameras, and a back light was installed in line with the drop camera. The drop camera, which had a 5.24 cm field of view and pixel resolution of 21 μm, was moved during the experiment to capture drops at elevations of 25 cm and 35 cm above the breaking wave crest. Drops sizes were computed from the imagery using a custom analysis routine, where the irregular background was removed, drop edges were identified, and their equivalent diameters (D) were calculated (Figure 2). Drops occurring on the edge of the image (i.e. not fully imaged) or not in focus were removed from consideration, and drops smaller than four pixels in diameter were not considered in the analysis. In the analysts presented in the next section drops histograms were computed using a log scale bins size.

Surface foam was measured with infrared imagers and visible-spectrum camera systems as previously employed to study waves in the laboratory [*Branch et al.*, 2013] and the field [*Jessup et al.*, 1997]. We will use the visible-spectrum camera to find the total whitecap area. Simultaneous in situ measurements of the TKE were made by sampling below the surface using a profiling acoustic Doppler velocimeter (ADV) and a single volume ADV. Near surface wave TKE dissipation rates will be calculated using the methods in *Thomson* [2012].

Other measurements included void fraction, and wave height. Void fraction was measured at three depths with custom impedance void fraction probes. The probes were calibrated prior to the experiment in a laboratory bubble chamber. During the experiment, the deepest void fraction probe failed and was not considered in the analysis. The time series of surface elevation was measured with ultrasonic distance meters approximately 5m down-wave of the spray and wave breaking measurements.

Analysis and Results

Analysis has focused on the drops observed in the camera imaging systems. Drops observed from the PDA are not presented or analyzed due to the low number of drops measured.

Preliminary analysis focused on combining observations from drop imaging data, plan view imagery of whitecap coverage, and in situ observations of wave energy dissipation rates and void fraction of the wave breaking bubble cloud. Figure 3 shows an example of a 20-second time series from a breaking wave event. This multi panel figure shows the drop camera, plan view of the wave breaking, drop size occurrence, void fraction, and wave TKE dissipation rate. The general pattern shows an expected sequence of events where the surface foamy coverage appears simultaneous to the registering of a bubbly plume past the shallow (10 cm depth) void probe. Approximately one second later a higher void fraction reading is evident at the deepest probe indicating a lag due to vertical and horizontal advection of the plume to this depth. The figure shows white cap coverage, intense energy dissipation, and near surface bubble plume presence lead the formation of a deep plume (40 cm) and ejected drops. Drops are still observed even 2 s after the initial event, and the elevated void fraction lasts for 4-5 s after the initial breaking.

The noisy signal of the observations is expected due to the non-linearity of wave breaking, and this property make interpretation of single realizations difficult. For example, the number of drops imaged during a single breaking event number less than 100. Therefore, the data were aggregated into ensemble averages. Temporal alignment of the data time series was achieved by correlation matching a wave height signal in the wave elevation and the white cap cover time series. Using both data sources was

necessary due to small offsets in the time series from each. A combination data plot in Figure 4 shows the ensemble data trends. Peaks in the TKE, ε, the rate of TKE dissipation, and the void fraction at 10 cm (neglecting the period when the instrument emerges in the wave trough) are in phase with the passage of the whitecap, while the void fraction at 40 cm depth lags approximately 1 s behind. This is presumably due to the time needed for the downward advection of the bubble plume generated from breaking.

Like the void fraction, the major peak in the detected drops occurs approximately 1 s after the whitecap passing, though the temporal distribution is broad (Figure 4e). The temporal drop distribution is shown in an expanded plot in Figure 5, and the whitecap fraction time series is plotted for reference with Figure 4. Just prior to the passage of the main breaker, only a few drops are seen, and the average drop size is close to 1 mm (Figure 5b). During the next phase, when the white cap passes through the measurement region between 0.5 and 2 s, the bolus of drops is imaged and the mean drop size increases from 200 to 300 μm during the time period. This is followed by a one second gap where only a few drops are imaged and then by another group of drops from 3.3 to 4.5 s, though the total number of drops at this time is an order of magnitude smaller than the first drop peak. The drop diameters in the latter group tend to be between 300 μm to 1 mm, and there is no clear trend with time. Figure 4c shows the difference in the mean drop size with time for the observations at 25 and 35 cm from the wave crest. In general, larger drops are observed at the higher location, though there is significant scatter, especially during times of sparse drop observations.

Using calibration imagery, we calculated the drop density for all the drops observed during the experiment that occurred during breaking. Figure 6a show the resulting drop density (per cubic meter) distribution. We find a characteristic two-part power law distribution where drops smaller than 1 mm have an approximately log-log space slope of -2 and for drops larger than 1 mm the log-log slope is -3.5, which matched well the recent data observed by *Erinin et al.* [2019]. Log-log slopes for measured drop distributions in literature span from -2.8 to -8 [*Wu et al*., 1984] and many slopes in between [e.g. *Veron et al*, 2012; *Watanabe and Ingram*, 2016]. Separated into observations from our two measurement heights we find slightly different distributions of drops. Primary, we find a lower overall drop count density at the higher elevation (35 cm) compared with the lower (25 cm). The shape of each distribution is similar, though the hinge point moves from $D \approx 1$ mm to $D \approx 1.7$, indicating a general coarsening of the drops. The drops distributions larger and smaller than this point still maintains a similar shape, though there is some indication of a slightly flatter distribution (-1.8) of finer drops at the higher (35 cm) observations.

Discussion and Conclusions

We note that the drops observed using our camera imaging technique are in the size class mostly considered "spume" drops, however the tearing of drops by wind [*Wu*, 1990; *Veron et al*., 2012], the mechanism that produces spume, is not present in our mechanically generated breaking waves. Instead we suspect that these drops are mainly produced by the breaking wave jet impact and turbulent splashing ubiquitous in a breaking wave. However, like spume drops, and different than jet or film drops, the expectation is that splash drops will not travel very far vertically since their initial velocity to do so would necessarily need to be large and their terminal fall velocity is also large, which results in a short-lived ballistic flight of durations less than a second. Spume drops are likely only travelling horizontally with the wind. As a result, measurements of splash drops have not been captured in the field due to the necessary close proximity to their generation in a breaking wave, thus out field-scale observations here are among the few splash drop measurements. Further evidence that we are likely measuring splash drops is the similarity of drop size distributions with the laboratory observations of wave-impact splash drops measured by *Watanabe and Ingram* [2016]. In their work, the find a wide range of drop size distribution in wave impacts with log-log slopes for drops larger than 0.7mm of -2 to -2.5, that while shallower than our observations, appears closer to what we observe than the -8 slope from *Wu et al*. [1984].

The break point in the slope of 1 mm is thought to be related to the Hinze scale observed in bubbles, where the bubbles larger than 1 mm are more prone to fragmentation due to turbulence, whereas the smaller bubbles are stabilized by surface tension [Hinze, 1955]. The stability of drops and their susceptibility to fragmentation is also noted in the literature of rain drop size measurements [e.g. *Villermaux and Bossa*, 2009; *Chou et al.*, 1997; *O'Rourke and Amsden*, 1987]. To look at this effect and to develop an explanation of our observed drop size distributions, we develop a simple ballistic model splash model based on a simple vertical-only drop trajectory with drag.

Our model assumes initial drop velocities, v_0, scale with the velocity inherent in the plunging jet, which is given by *Dazen et al*., [2008] as

$$v_0 = \sqrt{2gH} \tag{1}$$

where g is the gravitational acceleration and H is wave height. We assume that v_0 is Rayleigh distributed where $\langle v_0 \rangle = \sqrt{gH\pi}$. The probability that a drop has appropriate v_0 to be observed

$$P(v_0(z_{obs}, v_t) > v_{crit}) \tag{2}$$

is a function of the observation height, z_{obs}, and the measured drop size-dependent terminal velocity, v_t [*Foot and DuToit,* 1969], where the critical velocity, v_{crit} is

$$v_{crit} = \left[v_t^2\left(e^{2gz_{obs}/v_t^2} - 1\right)\right]^{\frac{1}{2}}. \quad (3)$$

For our experiment the wave height was 0.7 m and the resulting drop model shows that the flight characteristics (time aloft and maximum height) model vary significantly for a range of initial velocities and drop height, as plotted in Figure 7a,b. The probability of a given drop being observed based on (1)-(3) is shown in Figure 7d, where H = 0.65m. Over all, the probability of observing a drop decreases with increasing observation height above the water surface. As for the flight characteristics, there is also a notable and dramatic drop in the likelihood that a drop will be observed if it is smaller than 1 mm in diameter for observation heights above 0.5 cm, though this drop-off in probability moves to smaller drop sizes with decrease in the observation height. We can extend this model to attempt to predict the distribution of drop sizes we observed in our measurements by taking the product of a drop source function $F(D)$ with P, and here we choose $F(D) = kD^{-3.5}$, where k is a fitting constant. Plots of the resulting ballistics model for the total aggregate data set (Figure 8a) and the observations segregated by measurement height (Figure 8b). While the model matches the large drop distribution (D > 1 mm) it effectively predicts no drops to be observed for D < 1 mm. This mismatch coincides well with the break in the distribution slope at 1 mm, however it's unrealistic given the ubiquity of these small drops. The model does also predict a decrease in the number of drops seen at the higher observation height (with k constant), however the decreases is too small for D > 1 mm.

The lack of our ability to model the distribution of small drops indicates a range of possibilities, including an incorrect drop source function, incorrect parameter inputs, and missing flight physics. Since we are focused on prediction of the drop source function from first principals, we will look at the last two reasons. Our model relies on assumptions of the initial drop velocity and drop terminal velocity (i.e. drag). Of these two we are most likely to misrepresent the initial drop velocity, which though we scaled it with the wave jet velocity, we have not represented other drop ejection mechanism, especially though the pneumatic ejection that is often seen in the collapse of a plunging wave cavity. Much like a projectile this could easily launch drops of all sizes with a significant velocity. We could have also misrepresented the velocity distribution which would have to have a much larger fraction of high velocities, which in turn might be related to missing dynamics and physics. Of the missing physics, we do not consider the fragmentation, or break up, of drops once in flight. The splash impact measurements of *Watanabe and Ingram* [2016] and breaking wave measurements of *Erinin et al*. [2019] clearly document the breakup

or sheets, films, and ligaments into drops, though larger drops can also breakup in flight given significant velocity [e.g. *Villermaux and Bossa*, 2009 and *Flock et al*., 2012]. To assess the possibility of drop fragmentation in flight, which could increase the relative portion of smaller drops and decrease the number larger drops, we calculated the Weber number (*We*) which is the ration of aerodynamic shear stresses to surface tension, or

$$We = \frac{\rho_a D v^2}{\sigma} \tag{4}$$

where ρ_a is the density of air and σ is the surface tension. This is plotted in Figure 7c for a range of initial velocities. For *We* > 6-9 we expect fragmentation processes to start, however for the initial velocities we have plotted only the largest drops we measured would be likely to reach this threshold, indicating fragmentation is unlikely. Of course, we may need to measure the drops closer to formation (at the surface) to truly assess the fragmentation that has transpired.

Conclusions

We conducted field-scale observations of wave breaking and drop productions measured very near the surface (< 1 m) are among the first of its kind. Measurements of in situ properties including TKE, TKE dissipation rates, bubble imagers, and void fraction were contemporaneous with wave height time series, whitecap fraction, and drop size distribution in an effort to develop a near-surface drop source function, and to develop a better understanding of drop generation in breaking waves. Our observations were best suited to examining the timing and distribution of drops larger than 100 μm, often called spume and splash drops, which have significant effects on optical and EM properties in the marine boundary layer. Our results indicate that the drop distribution for drops from 100 μm to 1 cm are represented well by a two-part power law distribution with a log-log slope of -2 for drops from 100 μm to 1 mm and a slope of -3.5 from 1 mm to 1 cm. These distributions are in a general agreement with the few previously measured large drop distributions from laboratory experiments. We developed a drop ballistics model to described the observations with an initial drop velocity from wave velocity scaling and using previously measured drop terminal velocities. Our model can describe the location of the distribution slope change, but underestimates the number of drops for D < 1mm. We propose that an improved model will have to include drop fragmentation and have better representation of initial drop velocities.

References

Andreas, E. L., J. B. Edson, E. C. Monahan, M. P. Rouault, and S. D. Smith (1995). The spray contribution to net evaporation from the sea: A review of recent progress, *Bound.-Lay. Meteorol.*, *72*, 3-52.

Asher, W.E., and P.J. Farley (1995). Phase-Doppler anemometer measurement of bubble concentrations in laboratory-simulated breaking waves, *Journal of Geophysical Research, 100*, 7045-7056.

Asher, W. E., L. M. Karle, and B. J. Higgins (1997). On the differences between bubble-mediated air-water gas transfer in freshwater and seawater, *Journal of Marine Research, 55*, 813-845.

Branch, R., Chickadel, C., and Jessup, A. (2013). Thermal infrared multipath reflection from breaking waves observed at large incidence angles. Transactions on Geoscience and Remote Sensing, IEEE, PP(99):1–8.

Bauckhage, K. (1988), The Phase-Doppler-Difference-Method, a New Laser-Doppler Technique for Simultaneous Size and Velocity Measurements. Part 1: Description of the method. *Part. Part. Syst. Charact.*, 5: 16-22. doi:10.1002/ppsc.19880050105.

Callaghan, A. H. (2013). An improved whitecap timescale for sea spray aerosol production flux modeling using the discrete whitecap method. Journal of Geophysical Research: Atmospheres, 118(17):9997–10,010.

Callaghan, A. H., Deane, G. B., and Stokes, M. D. (2013). Two regimes of lab- oratory whitecap foam decay: Bubble-plume controlled and surfactant stabilized. Journal of Physical Oceanography, 43(6):1114–1126.

Chou, W.-H., Hsiang, L.-P., and Faeth, G. M. (1997) Temporal properties of drop breakup in the shear breakup regime, *International Journal of Multiphase Flow, 23*, 4. doi:/10.1016/S0301-9322(97)00006-2.

Deane, G. B. and Stokes, M. D. (2002). Scale dependence of bubble creation mechanisms in breaking waves. Nature, 418(6900):839–844.

Erinin, M. A., Wang, S. D., Liu, R., Towle, D., Liu, X., and Duncan, J. H. (2019) Spray generation by a plunging breaker, *Geophysical Research Letters*, 46, 14. doi:/10.1029/2019GL082831.

Flock, A.K., D.R. Guildenbecher, Chen J., P.E. Sojka, and H.J. Bauer (2012) Experimental statistics of droplet trajectory and air flow during aerodynamic fragmentation of liquid drops. *Int. J. Multiph. Flow*, 47, pp. 37-49.

Göbel, G., T. Wriedt, and K. Bauckhage (1998). Micron and submicron aerosol sizing with a standard phase-Doppler anemometer, *Journal of Aerosol Science, 29* (9), 1063-1073.

Geever, M., O'Dowd, C. D., van Ekeren, S., Flanagan, R., Nilsson, E. D., de Leeuw, G., and Rannik, U¨. (2005). Submicron sea spray fluxes. Geophysical Research Letters, 32(15)

Hinze, J. O. (1955) Fundamentals of the hydrodynamic mechanism of splitting in dispersion processes. *AIChE J.* 1 (3), 289–295.

Jessup, A. T., Zappa, C. J., Loewen, M. R., and Hesany, V. (1997). Infrared remote sensing of breaking waves. Nature, 385(6611):52–55.

Martensson, E. M., Nilsson, E. D., de Leeuw, G., Cohen, L. H., and Hansson, H.-C. (2003). Laboratory simulations and parameterization of the primary marine aerosol production. Journal of Geophysical Research, 108(D9):4297.

Monahan, E. C., D. E. Spiel, and K. L. Davidson (1986). A model of marine aerosol generation via whitecaps and wave disruption, in Oceanic White- caps, edited by E. C. Monahan and G. MacNiochaill, pp. 167–193, D. Reidel, Norwell, Mass.

Naqwi, A., and M. Ziema (1992). Extended phase Doppler anemometer for sizing particles smaller than 10 micrometers, *Journal of Aerosol Science, 23* (6), 613-621.

Nilsson,E.D., Rannik,U., Swietlicki,E., Leck,C., Aalto,P.P., Zhou,J., and Norman, M. (2001). Turbulent aerosol fluxes over the Arctic Ocean: 2. Wind-driven sources from the sea. Journal of Geophysical Research: Atmospheres, 106(D23):32139–32154.

O'Rourke, P. J. and Amsden, A. A. (1987) The tab method for numerical calculation of spray droplet breakup, doi:/10.4271/872089.

Qiu, H.H., and M. Sommerfeld (1992). A reliable method for determining the measurement volume size and particle mass fluxes using phased-Doppler anemometry, *Experiments in Fluids, 13*, 393-404.

Rapp, R. J. and Melville, W. K. (1990) Laboratory measurements of deep-water breaking waves, *Philosophical Transactions of the Royal Society of London. Series A, Mathematical and Physical Sciences, 331*, 1622. doi:/10.1098/rsta.1990.0098.

Thomson, J. (2012) Wave breaking dissipation observed with 'SWIFT' drifters, *Journal of Atmospheric and Oceanic Technology, 29,* doi:/10.1175/JTECH-D-12-00018.1.

Petelski, T., and J. Piskozub (2006), Vertical coarse aerosol fluxes in the atmospheric surface layer over the North Polar Waters of the Atlantic, *J. Geophys. Res.*, 111, C06039.

Veron, F., Hopkins, C., Harrison, E. L., and Mueller, J. A. (2012) Sea spray spume droplet production in high wind speeds, *Geophysical Research Letters, 39,* 16. doi:/10.1029/2012GL052603.

Villermaux, E. and Bossa, B. (2009) Single-drop fragmentation determines size distribution of raindrops, *Nature Physics, 5,* doi:/10.1038/nphys1340.

Watanabe, Y. and Ingram, D. M. (2016) Size distributions of sprays produced by violent wave impacts on vertical sea walls, *Proceedings of the Royal Society of London A: Mathematical, Physical and Engineering Sciences, 472,* 2194. doi:/10.1098/rspa.2016.0423.

Wu, J. (1990) Vertical distributions of spray droplets near the sea surface: influences of jet drop ejection and surface tearing, *Journal of Geophysical Research: Oceans, 95,* C6. doi:/10.1029/JC095iC06p09775.

Wu, J., Murray, J. J., and Lai, R. J. (1984) Production and distributions of sea spray, *Journal of Geophysical Research: Oceans, 89,* C5. doi:/10.1029/JC089iC05p08163.

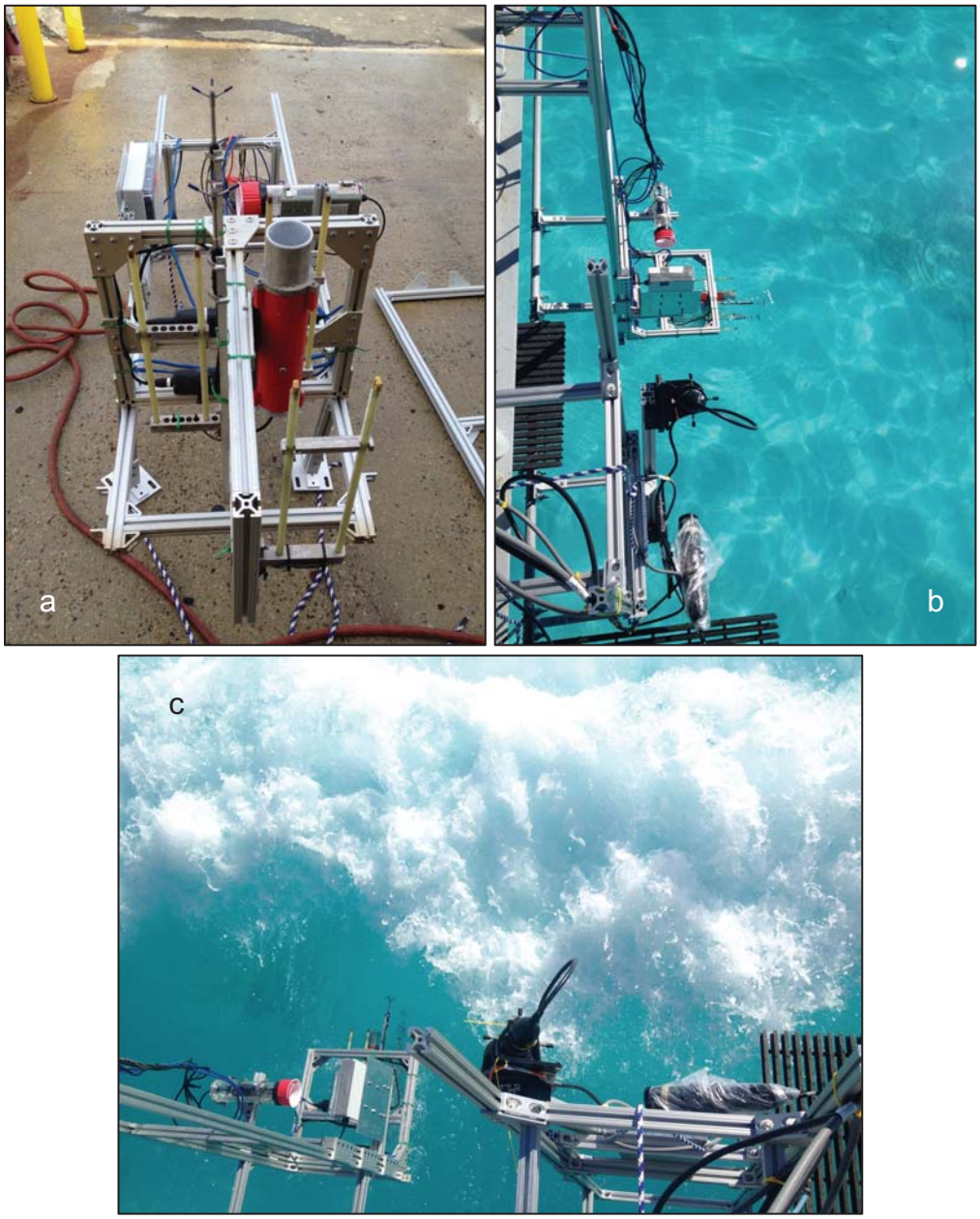

Figure 1. (a) In water sensor array including ADVs, void probes and camera. (b) PDA (bottom part of picture) and in water sensors attached to the instrument bridge in the wave flume. (c) a breaking wave about to pass though the sensor array.

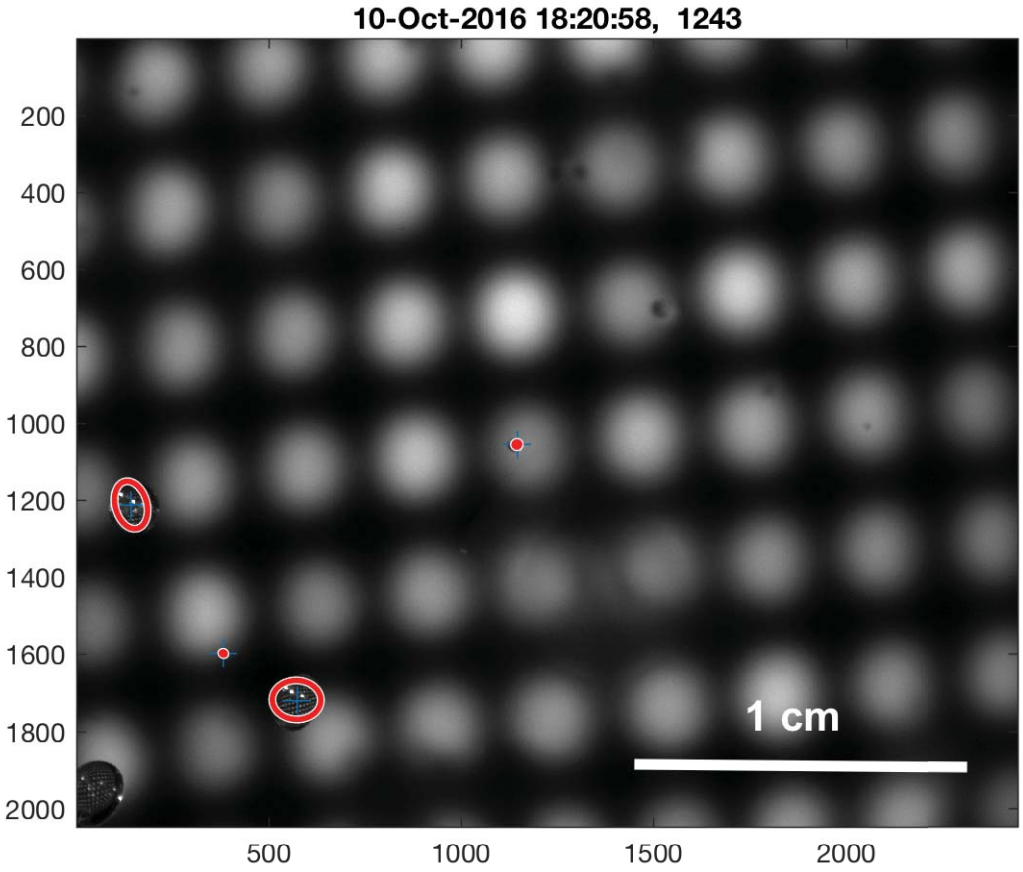

Figure 2. An example droplet imaging processing result. The patterned background is the due to the LED backlight, and the identified drops that are in focus and fully in the image frame are circled in red.

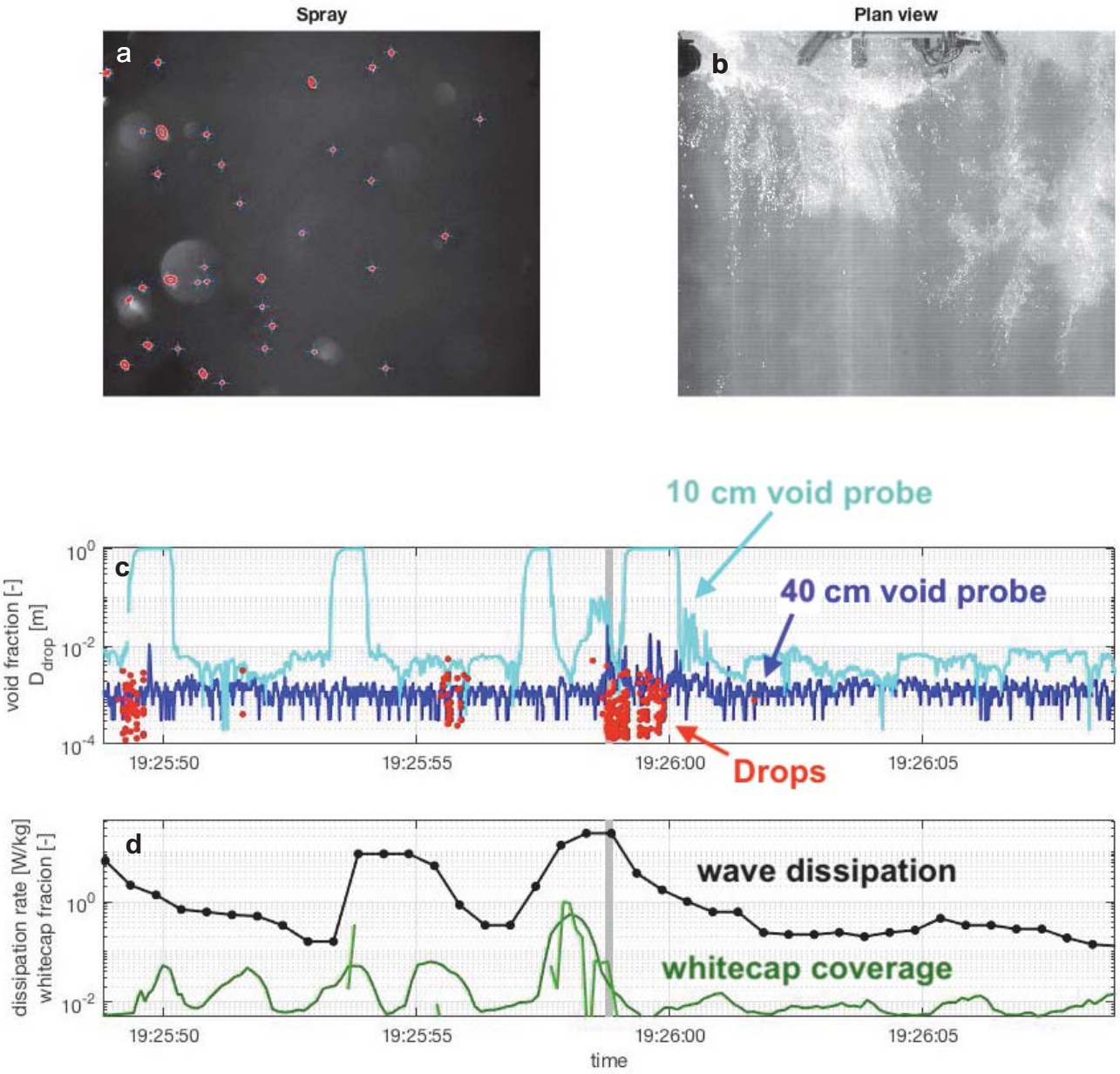

Figure 3. a) Drops identified in the droplet camera, and b) plan view of the wave breaking during a breaking event. c) The void fraction and droplet incidence show the lag in both the bobble cloud at depth and the resulting drop formation relative to the d) peaks in whitecap coverage wave energy dissipation, which are fairly simultaneous. Droplets are observed up to 2 seconds after the initial formation of the wave event.

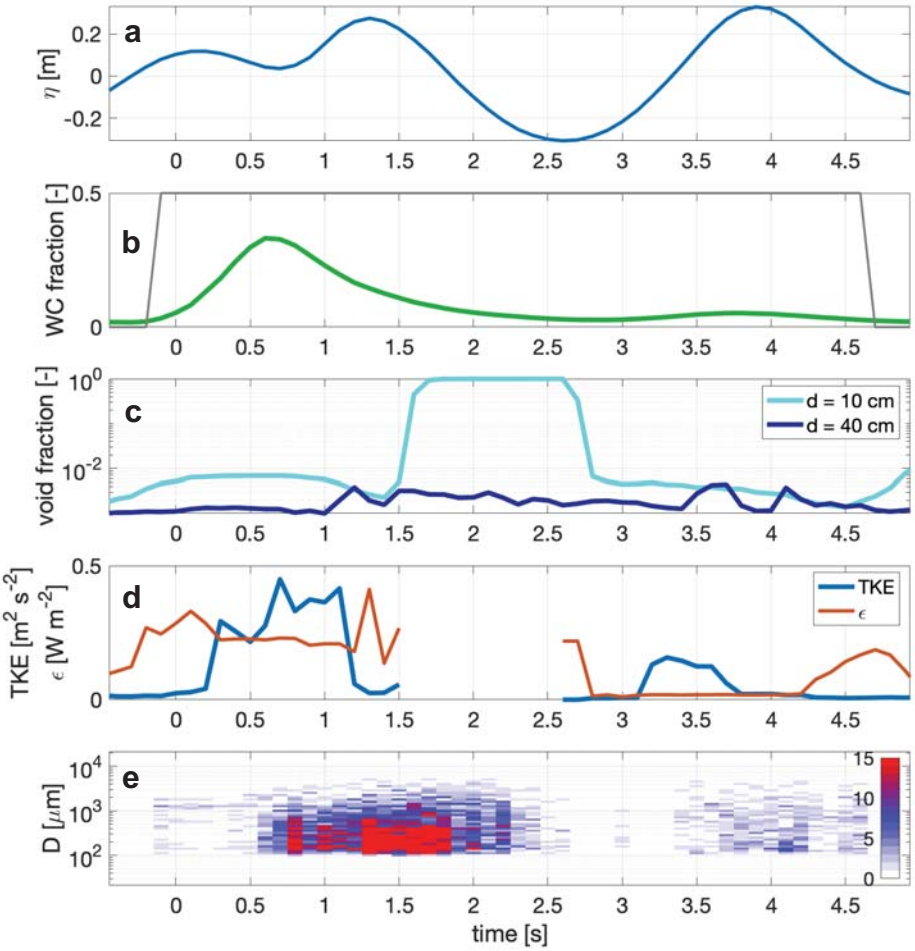

Figure 4. Time series of the ensemble composite data. a) Surface elevation time series. b) Whitecap fraction coverage. c) Void fraction at 10 and 40 cm, depth from the still water, note that the 10 cm measurement is exposed during the passage of the wave trough and indicates 100% void fraction. d) TKE and TKE dissipation rate, ε. e) average drop size count histogram time series.

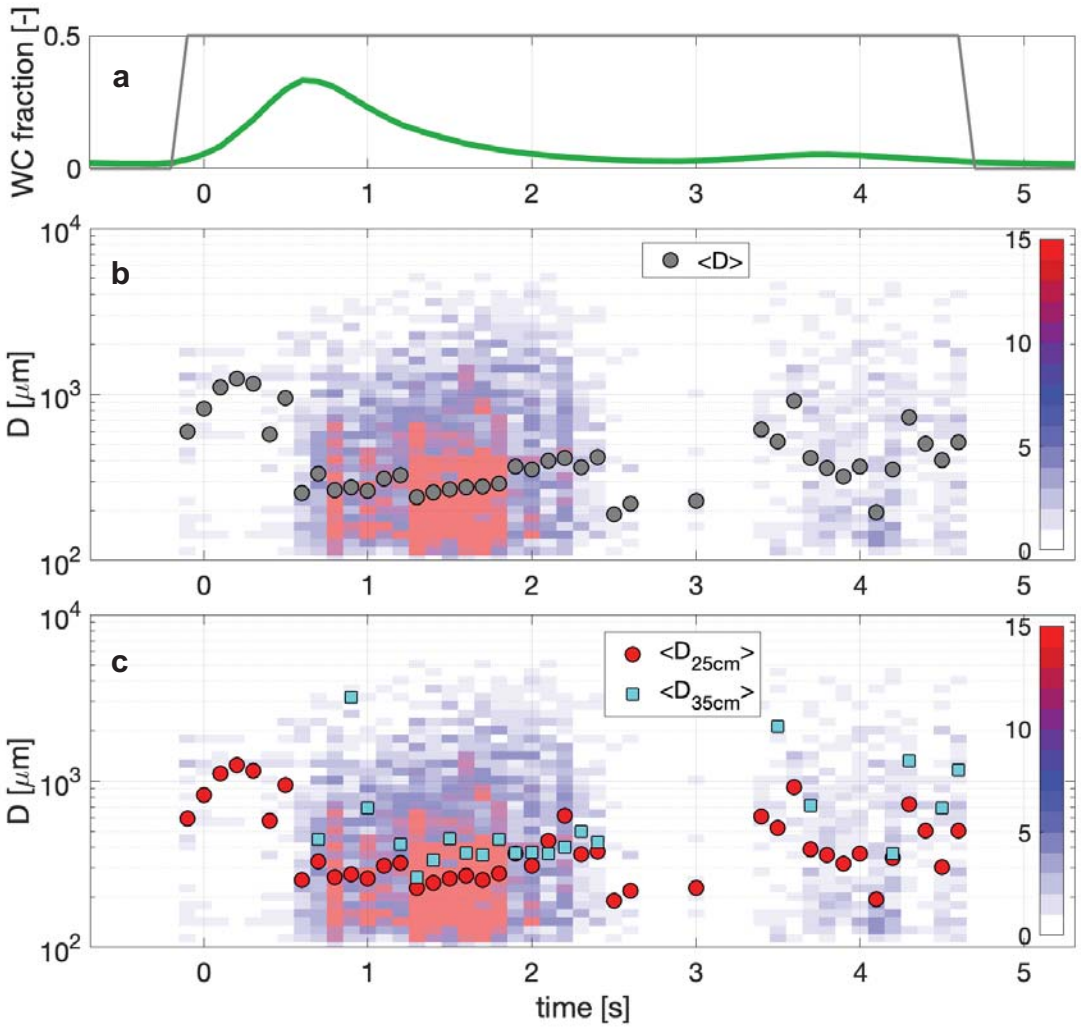

Figure 5. a) Time series of the ensemble averaged white cap fraction. b) Time series histogram of drop sizes with the mean drop size indicated. c) Time series histogram of drop sizes with the mean drop size indicated for observations from 25 cm (red circles) and 35 cm (blue squares) above the wave crest height.

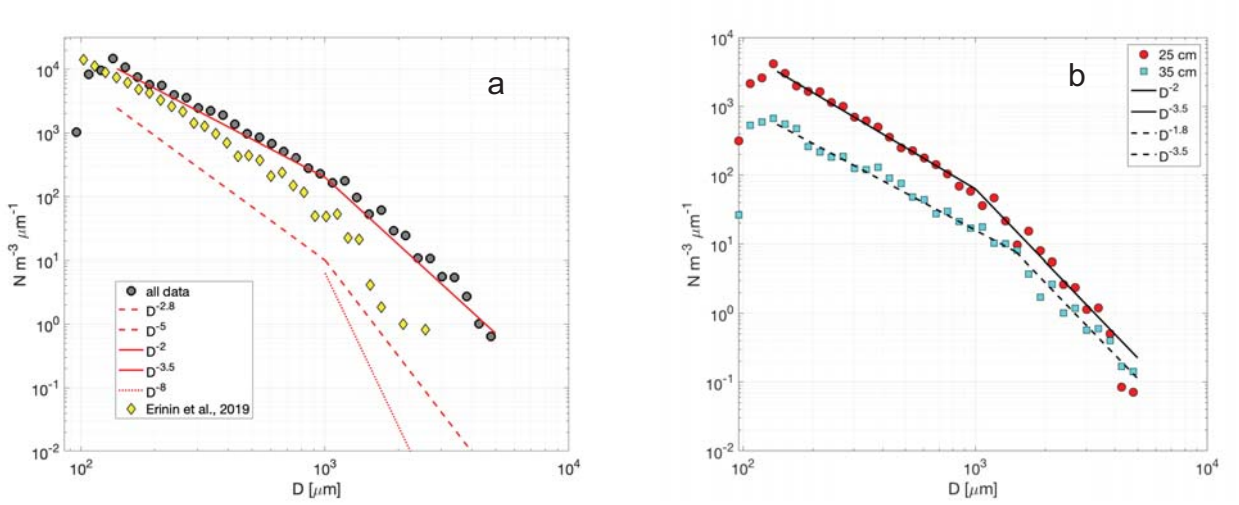

Figure 6. a) Drops per m^3 density histogram (gray circles) for the data measured in the experiment. Yellow diamonds indicate a scaled probability density plot of drops sizes observed in a laboratory breaking wave by *Erinin et al.* [2019], showing similarity to our measurements. The red lines indicate power law distribution functions that best fit the data (solid lines) and others observed and proposed (dashed and dotted lines). b) Drop per m^3 density histograms of data observed here, but separated by observation height relative to the maximum crest height. Approximate power law fits are indicated (solid and dashed lines).

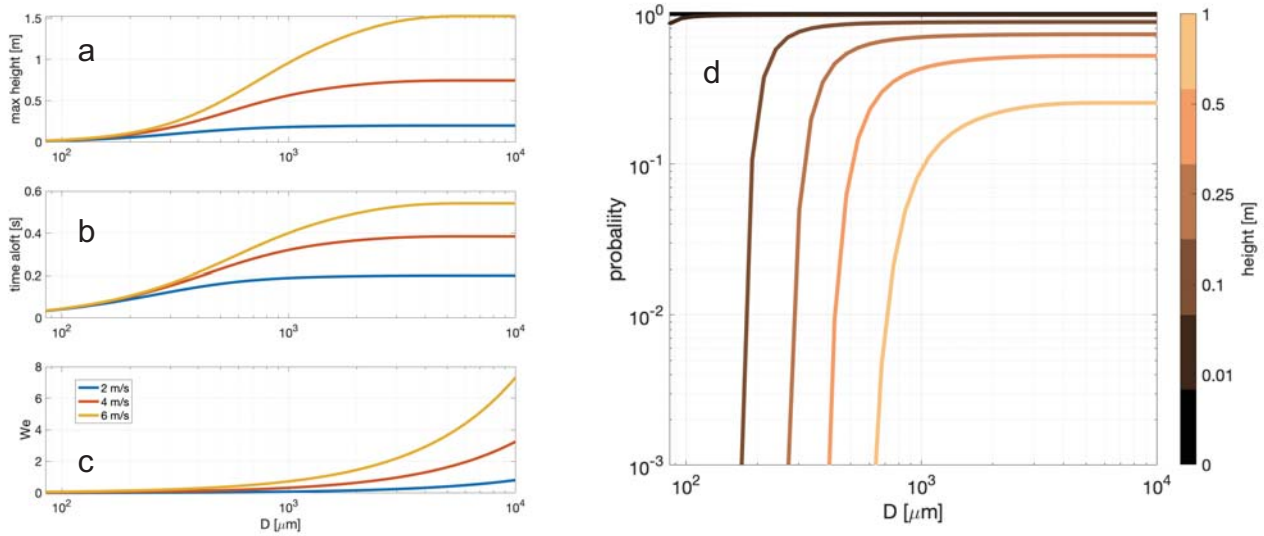

Figure 7. Drop flight characteristics calculated from the vertical ballistics model with drag: (a) maximum height and (b) time aloft, plotted for three different initial velocities, 2 4, and 6 m/s. (c) The Weber number is calculated for the same drop sizes and initial velocity as in (a) and (b). The probability of observation of a given drop size is plotted for different observations heights z_{obs}.

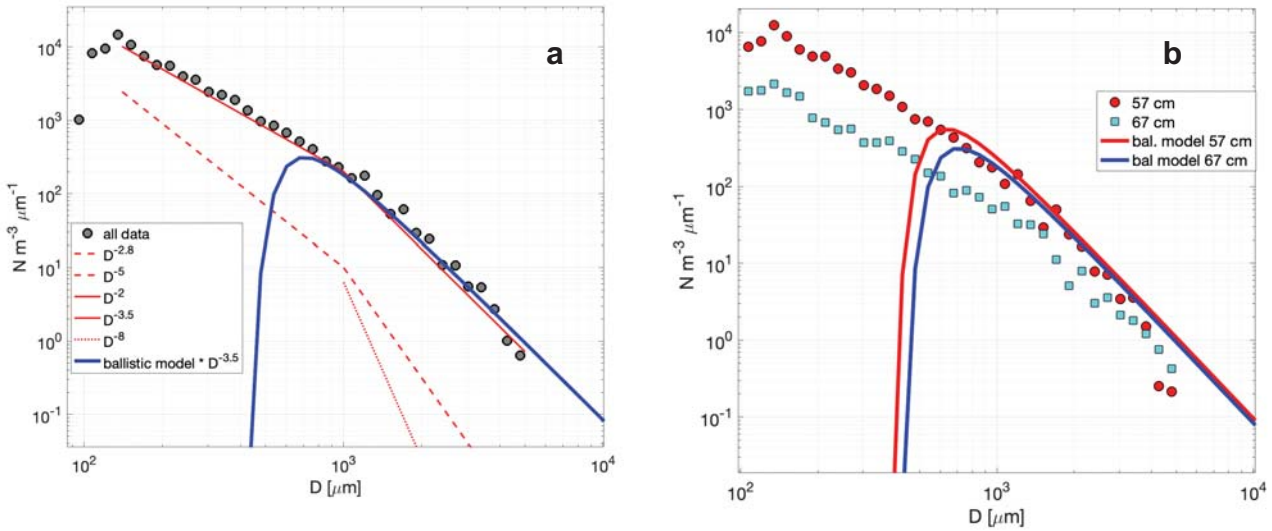

Figure 8. (a) Plot of the ballistic model for the average observed height and the measured drop observed density. (b) comparison of the ballistic model with data from the two observations heights.

REPORT DOCUMENTATION PAGE

Form Approved
OMB No. 0704-0188

1. REPORT DATE *(DD-MM-YYYY)*	2. REPORT TYPE	3. DATES COVERED *(From - To)*
09/19/2019	Final Technical Report	07/01/2019 - 06/30/2019

4. TITLE AND SUBTITLE
Spray Production and Surface Foam Longevity under Breaking Waves

5a. CONTRACT NUMBER

5b. GRANT NUMBER
N00014-15-1-2719

5c. PROGRAM ELEMENT NUMBER

6. AUTHOR(S)
C. Chris Chickadel
William Asher

5d. PROJECT NUMBER

5e. TASK NUMBER

5f. WORK UNIT NUMBER

7. PERFORMING ORGANIZATION NAME(S) AND ADDRESS(ES)
Applied Physics Laboratory
University of Washington
1013 NE 40th Street
Seattle, WA 98105

8. PERFORMING ORGANIZATION REPORT NUMBER

9. SPONSORING/MONITORING AGENCY NAME(S) AND ADDRESS(ES)
Steven Russell (Code 331)
ONR SHIP SYSTEMS & ENGINEERING DIV
875 N. Randolph Street
Arlington, VA 22203-1995

10. SPONSOR/MONITOR'S ACRONYM(S)
ONR

11. SPONSOR/MONITOR'S REPORT NUMBER(S)

12. DISTRIBUTION/AVAILABILITY STATEMENT
Approved for public release; distribution is unlimited.

13. SUPPLEMENTARY NOTES

14. ABSTRACT
We conducted field-scale observations of wave breaking and drop productions measured very near the surface (< 1 m) to develop a better understanding of drop generation in breaking waves. Our results indicate that the drop distribution for drops from 100 m to 1 cm are represented well by a two-part power law distribution with a log-log slope of -2 for drops from 100 m to 1 mm and a slope of -3.5 from 1 mm to 1 cm. We developed a drop ballistics model to described the observations with an initial drop velocity from wave velocity scaling and using previously measured drop terminal velocities. Future work will need to better define drop initial velocities and drop fragmentation.

15. SUBJECT TERMS
spray, breaking waves, bubbles, drops, splash drops, sea foam, turbulence

16. SECURITY CLASSIFICATION OF:			17. LIMITATION OF ABSTRACT	18. NUMBER OF PAGES	19a. NAME OF RESPONSIBLE PERSON
a. REPORT	b. ABSTRACT	c. THIS PAGE			C. Chris Chickadel
U	U	U	U	19	19b. TELEPHONE NUMBER *(Include area code)* (206) 221-7673